RASĀYAN *J. Chem.*
Vol. 18 | No. 4 | 2521-2530 | October-December | 2025
ISSN: 0974-1496 | e-ISSN: 0976-0083 | CODEN: RJCABP
http://www.rasayanjournal.com
http://www.rasayanjournal.co.in

SYNTHESIS OF BIS-BENZIMIDAZOLE VIA CUBR/TTCA CATALYSIS: A COMBINED EXPERIMENTAL AND COMPUTATIONAL STUDY

Lalima Sharma[1], Siddhima Sharma[1], Sonia Chahar Srivastava[2,✉] and Mangal Shree Dulawat[1]

[1]Department of Chemistry, J.R.N. Rajasthan Vidyapeeth (Deemed to be) University, Udaipur, -313001, (Rajasthan), India

[2]Department of Chemistry, S.S. Jain Subodh College, Jaipur-302004, (Rajasthan), India,

✉Corresponding author: soniachahar@gmail.com

ABSTRACT

An efficient one-pot method was established for synthesizing 1,4-bis(1H-benzo[d]imidazol-2-yl) benzene using copper(1) bromide as a catalyst and trichloroisocyanuric acid as a mild oxidant under ambient conditions. The compound was structurally characterized by various spectroscopic techniques. Hirshfeld surface analysis and interaction energy calculations based on crystallographic data revealed that dispersion interactions dominate the crystal packing, supported by C···H and N···H contacts. The study highlights both the synthetic utility and the supramolecular properties of the title compound, offering valuable insights for materials and pharmaceutical research.

Keywords: Bis-Benzimidazole, Hirshfeld Surface Analysis, Intermolecular Interaction Energy, Crystal Packing.

RASAYAN *J. Chem.,* Vol. 18. No. 4, 2025

INTRODUCTION

Benzimidazole derivatives constitute an important class of nitrogen-containing heterocycles with widespread applications in medicinal chemistry, material science, and catalysis due to their remarkable biological activities and unique physicochemical properties.[1–3] Among these, 1,4-bis(1H-benzo[d]imidazol-2-yl)benzene (BBIB) and related bis-benzimidazoles have attracted significant attention in the design of advanced functional and pharmaceutical compounds.[4–12] Consequently, the development of efficient, sustainable, and green synthetic methodologies for bis-benzimidazoles remains a vibrant area of research.

Traditional synthetic routes to bis-benzimidazoles typically involve multistep procedures including condensation of o-phenylenediamine with aromatic dialdehydes, followed by oxidative aromatization under harsh conditions using stoichiometric amounts of oxidants. These methods often suffer from long reaction times, low atom economy, and environmental concerns related to the use of toxic reagents or heavy metals.[13,14] Recent advances have focused on tandem one-pot protocols that integrate condensation, cyclization, and oxidation steps to streamline synthesis while enhancing efficiency and reducing waste. In this context, copper(I) bromide (CuBr) has emerged as an attractive Lewis acid catalyst capable of activating carbonyl substrates to facilitate condensation and cyclization reactions under mild conditions.[15–17] Concurrently, Trichloroisocyanuric Acid (TTCA) is known to be a mild and selective organic oxidant, enabling efficient oxidative aromatization without requiring harsh or hazardous conditions.[18–20] Herein, we report a novel, efficient, and green one-pot synthetic approach for the preparation of BBIB via CuBr-catalyzed condensation and cyclization of o-phenylenediamine with terephthalaldehyde, followed by TTCA-mediated oxidative aromatization. This tandem catalytic system operates under mild reaction conditions with excellent yields and high selectivity, providing an environmentally benign alternative to conventional protocols. The synthesized compound was examined using Nuclear Magnetic Resonance (NMR) spectroscopy, Fourier Transform Infrared (FTIR) spectroscopy, and Mass Spectrometry (MS) to validate its structure and confirm the absence of impurities. The synthesized BBIB compound was further investigated using computational chemistry techniques to understand its intermolecular interactions. Hirshfeld surface analysis & interaction energy calculations

http://doi.org/10.31788/RJC.2025.1849390

were executed using the crystallographic information file (CIF) data, following established methodologies. These analyses were carried out in this study because the intermolecular interaction profile of the compound had not been previously explored. The findings offered clear information about the type and intensity of intermolecular interactions, helping to better understand the compound's supramolecular properties and overall stability.

EXPERIMENTAL

Materials and Methods

The compound BBIB was synthesized using reagents and solvents acquired from Sigma-Aldrich. Thin-layer chromatography (TLC), with silica gel plates supported on aluminium, was used to assess the reaction.

General Procedure

In a typical reaction setup, terephthalaldehyde (1 mmol), o-phenylenediamine (2 mmol), and copper(I) bromide (10 mol%) were combined in 10 mL of ethanol and stirred using a magnetic stirrer. The mixture was then refluxed for 2 hours to drive the condensation and ring-forming process. After the solution was brought down to 25 °C, TTCA (1.2 mmol) was introduced gradually in small portions, and stirring was maintained for an additional 3 hours to complete the oxidative aromatization. The transformation was tracked by TLC in DCM: MeOH (9:1). Upon full conversion, the reaction was quenched by pouring into chilled water, resulting in the precipitation of a solid. Post filtration of the product, it was washed with water. Ethanol used for recrystallization yielded the BBIB compound in pure form (Yield 83%, m.p. 193 °C) .

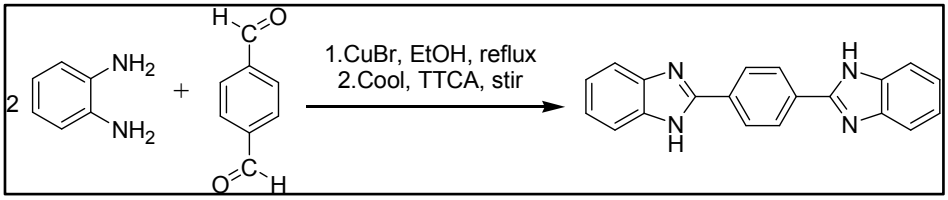

Fig.-1: Scheme for the Synthesis of BBIB

Synthesis of Bis-benzimidazole

The reaction mechanism begins with copper(I) bromide acting as a Lewis acid catalyst by coordinating to the carbonyl oxygen atoms of terephthalaldehyde, thereby increasing their electrophilicity (Fig.-1). This activation enables the primary amine groups of o-phenylenediamine to perform a nucleophilic attack, resulting in the creation of a bis-imine intermediate via the loss of water. Subsequently, the adjacent amine groups intramolecularly attack the imine carbons, promoting cyclization and generating a bis-dihydrobenzimidazole intermediate. Throughout these steps, CuBr may stabilize reactive intermediates via coordination. In the final stage, TTCA serves as a mild oxidizing agent, promoting the oxidative dehydrogenation of the dihydrobenzimidazole rings. This oxidation step restores aromaticity to both benzimidazole units, furnishing the target BBIB. The tandem catalytic action of CuBr and TTCA thus enables an efficient, one-pot synthesis under mild reaction conditions by seamlessly integrating condensation, cyclization, and aromatization processes.

Detection Methods

Detection of the reaction progress was carried out under UV light (wavelength, 254 nm). The melting point of the final product was measured by Microprocessor Melting Point Apparatus (Model S-972). Infrared (IR) spectra were evaluated on a PerkinElmer Spectrum Two FTIR spectrometer to identify functional group vibrations within the molecule. Nuclear Magnetic Resonance (NMR) spectroscopy was used for structural analysis, with both ^{1}H &^{13}C NMR spectra performed on a Bruker Avance Neo 500 MHz spectrometer. To confirm the molecular formula and exact mass of BBIB, HRMS was determined using a Waters Synapt XS HDMS system. Hirshfeld Surface and Interaction Energy Analysis Hirshfeld surface analysis of BBIB was performed using CrystalExplorer17.5.The CIF file for computational analysis was obtained from the Cambridge Crystallographic Data Centre (CCDC), reference number 103999.[21][22] The surfaces were mapped over *dnorm* to visualize intermolecular contacts, and fingerprint plots quantified interaction contributions. Pairwise interaction energies were calculated at the

B3LYP/6-31G(d,p) level. Energy frameworks were constructed to illustrate dominant stabilizing forces in the crystal structure.[23,24]

RESULTS AND DISCUSSIONS

Structural Confirmation

FTIR

The FTIR spectrum of the synthesized bis-benzimidazole derivative exhibits characteristic vibrational bands that corroborate its proposed molecular structure. A prominent absorption at 3429 cm^{-1} is attributed to N–H stretching, consistent with the presence of secondary amine functionalities. The bands observed at 1634 cm^{-1} and 1439 cm^{-1} represent the aromatic C=C and azomethine (C=N) stretching vibrations, respectively, affirming the incorporation of benzimidazole moieties. Furthermore, the absorption at 1321 cm^{-1} is ascribed to C–N stretching, supporting the existence of a conjugated heteroaromatic framework (Fig.-2). The ^{1}H NMR spectrum (500 MHz, DMSO-d_6) of the bis-benzimidazole derivative reveals key resonances consistent with its aromatic and heterocyclic structure. A singlet at δ 8.4 ppm (4H) corresponds to the aromatic protons of the benzimidazole moieties, while multiplets at δ 7.7–7.6 ppm (4H) and δ 7.3–7.2 ppm (4H) are attributed to protons on the substituted phenyl rings. Additionally, a singlet at δ 4.00 ppm (2H) is assigned to the NH protons, confirming the presence of secondary amine groups in the molecule (Fig.-3).

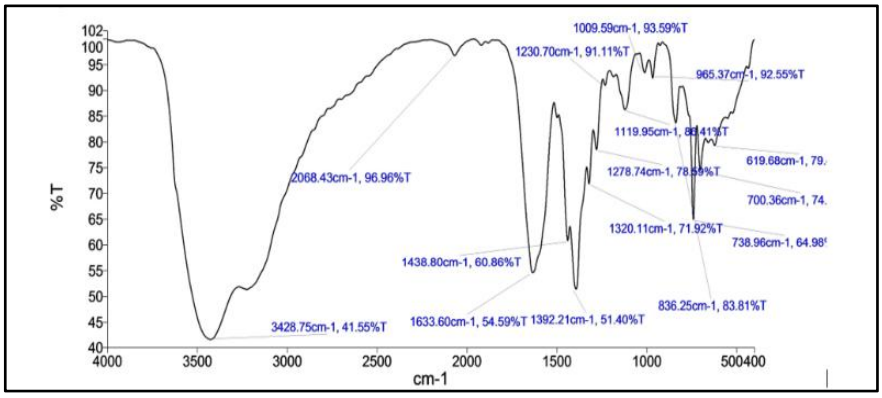

Fig.-2: FTIR Spectrum

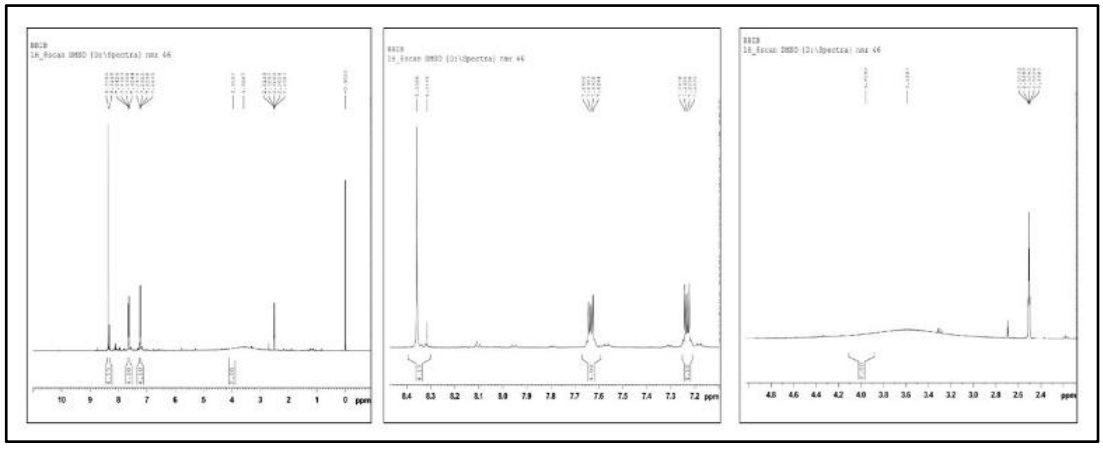

Fig.-3: ^{1}HNMR Spectrum

^{13}CNMR

The ^{13}C NMR spectrum (125 MHz, DMSO-d_6) of the bis-benzimidazole derivative displays resonances characteristic of both benzimidazole and phenyl carbons. Signals at δ 115 and 119 ppm are attributed to aromatic carbons within the benzimidazole rings, while peaks at δ 126 and 133 ppm correspond to the substituted phenyl ring carbons. Deshielded signals at δ 143 and 155 ppm are assigned to quaternary carbons of the benzimidazole units, likely adjacent to nitrogen atoms, supporting the integrity of the conjugated heteroaromatic framework (Fig.-4).

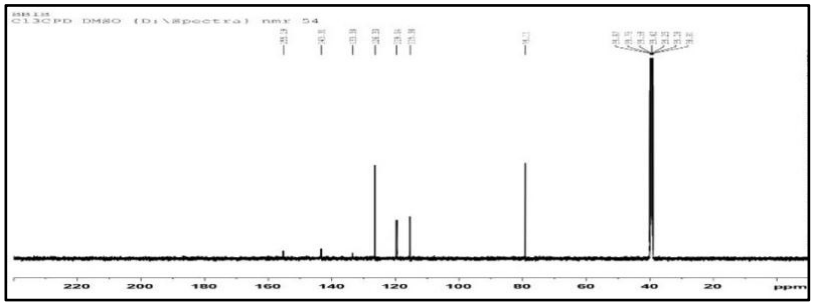

Fig.-4: ^{13}CNMR Spectrum

Mass Spectrum

The ESI$^+$ mass spectrum of the bis-benzimidazole derivative exhibits a molecular ion peak at *m/z* 311.14, which is in excellent agreement with the calculated value of *m/z* 311.13 for the protonated molecular ion $[M+H]^+$, consistent with the molecular formula $C_{20}H_{14}N_4$. This confirms the expected molecular weight and supports the proposed structural composition of the compound (Fig.-5).

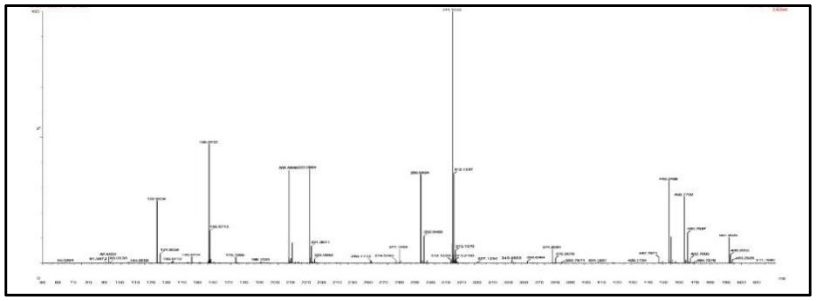

Fig.-5: Mass Spectrum

Hirshfeld Surface Analysis

Figure-6 Hirshfeld surface mapped over d_norm for BBIB, showing overall and decomposed intermolecular interactions. Top: Hirshfeld surface (left) and full 2D fingerprint plot (right) encompassing all contacts. Bottom: Decomposed surfaces and plots for H-- H (41.9%); C- -H/H/-C (35.4%); and N--H/H- -N (14.8%) interactions, illustrating their relative contributions to crystal packing. To gain detailed insight into the intermolecular interactions governing the crystal packing of the synthesized compound, a comprehensive Hirshfeld surface analysis was carried out. The *dnorm*-mapped Hirshfeld surface (Fig.-6) reveals important close interactions, with red areas indicating contacts shorter as compared to the combined van der Waals radii, white areas showing contacts near van der Waals distances, and blue areas marking longer-range interactions. The overall 2D fingerprint plot (Fig.-2, top right) encompasses all intermolecular contacts, providing a quantitative breakdown of the types and relative contributions of interactions. The decomposed fingerprint plots further reveal the dominance of specific interactions contributing to the crystal packing. The most significant interaction was found to be H···H contacts, accounting for 41.9% of the total Hirshfeld surface area. These interactions are typically non-directional and stem from close-packing arrangements, contributing to van der Waals stabilization in the solid state. The corresponding fingerprint plot shows a broad, symmetric region centered around 1.2–1.4 Å in both *di* and *de*, consistent with typical hydrogen–hydrogen interactions. The next most prevalent interaction type was C···H/H···C contacts, comprising 35.4% of the surface area. These interactions indicate the presence of weak C–H···π interactions, likely involving the aromatic rings within the molecular scaffold. The decomposed plot displays characteristic wing-like spikes that reflect the directional nature of these interactions. Notably, N···H/H···N interactions contributed 14.8%, reflecting potential hydrogen bonding between nitrogen lone pairs and nearby hydrogen atoms. Reddish spots present on *dnorm* surface are localized near the nitrogen atoms, indicating their role as acceptors in weak hydrogen bonds. The associated fingerprint plot reveals sharp spikes, characteristic of such specific and directional interactions. These results suggest that while dispersive H···H interactions dominate the crystal packing, C···H and

N···H contacts provide crucial directional stabilization, influencing molecular orientation and packing efficiency in the crystalline state.

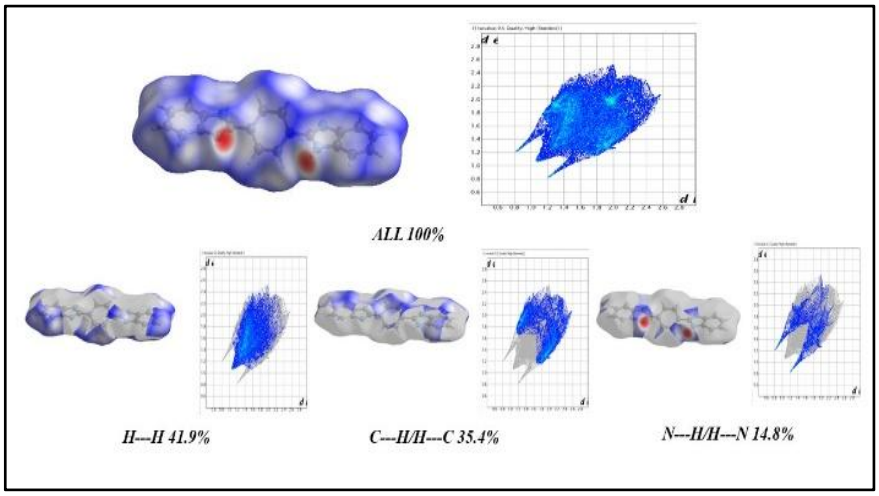

Fig.-6: Hirshfeld Surface Mapped Over d_norm for BBIB, Showing Overall and Decomposed Intermolecular Interactions. Top: Hirshfeld Surface (Left) And Full 2D Fingerprint Plot (Right) Encompassing All Contacts. Bottom: Decomposed Surfaces and Plots For H- -H (41.9%); C- -H/H- -C (35.4%); And N- -H/H- -N (14.8%) Interactions, Illustrating their Relative Contributions to Crystal Packing

Topological and Geometric Analysis

To further analyze the crystal packing and surface topology of the synthesized compound, several surface property maps were created, including di, de, shape index, curvedness, and fragment patches (Fig.-7). These maps provide nuanced insights into the nature and topology of intermolecular contacts. The *di* (distance internal) surface reveals regions where atoms inside the surface (i.e., from the molecule itself) come close to external atoms of neighboring molecules. For this molecule, the *di* surface shows intense red spots near the amine hydrogen and nitrogen atoms, indicating their participation in close intermolecular contacts, likely N–H···π or N–H···N interactions. Conversely, the *de* (distance external) surface displays the distance from the surface to atoms outside it. The reddish regions seen near the aromatic rings and nitrogen atoms indicate that electron-rich groups or hydrogen-containing groups are positioned nearby. This supports the idea that hydrogen bonding and π–π stacking interactions are taking place in those areas. The fragment patch surface delineates the molecular surface into various segments based on atomic connectivity and spatial proximity. For this fused-ring molecule, the patches correspond to distinct aromatic units, such as the phenyl ring and the benzimidazole moiety. This visualization aids in understanding how each structural component contributes to the molecular recognition and packing environment. In crystal packing, these fragments may align with similar units from neighboring molecules, facilitating π–π interactions and layered stacking motifs. The shape index surface provides a qualitative view of the surface topography, especially useful in identifying aromatic π···π interactions. Red and blue triangle-like regions on this surface signify complementary convex and concave surfaces involved in stacking. These features are pronounced around the benzimidazole and substituted phenyl rings in the molecule, confirming their role in face-to-face interactions essential for lattice stabilization. The curvedness surface captures variations in surface curvature. Low curvedness (green regions) indicates flat areas conducive to π-stacking, which is observed on the planar aromatic systems of the molecule. High curvedness (blue ridges) is seen around the nitrogen atoms and fused ring junctions, reflecting sterically hindered, less interactive regions. Together, these surfaces present a holistic visualization of how the molecule interacts within its crystal lattice. The red zones on *di* and *de* surfaces align with sites of high intermolecular contact, shape index confirms π–π stacking, and curvedness maps distinguish between interactive and inert surface zones. The rich aromaticity and presence of multiple nitrogen atoms facilitate strong directional interactions such as hydrogen bonding and stacking, which dominate the packing behavior of this molecule in the solid state. Such detailed surface analysis provides critical input

for understanding the molecule's stability, solubility, and potential binding interactions in supramolecular or biological contexts.

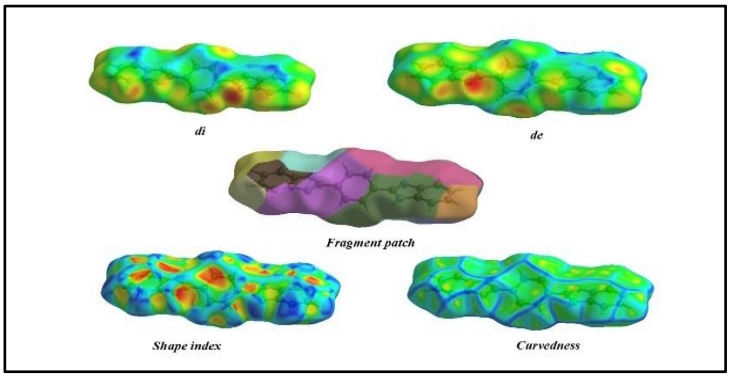

Fig.-7: Molecular Surface Property Maps Depicting Interaction Distances, Shape, Curvature, and Fragment Regions

Intermolecular Interaction Energy Calculations

Understanding the nature and strength of intermolecular interactions is crucial for elucidating the stability and packing of molecules in a crystal lattice. The results, expressed in kilojoules per mole (kJ/mol), offer insight into how individual molecules interact within the crystal structure.

Energy Components and Their Significance

Each interaction energy between a pair of molecules is broken down into four major components, each representing a different physical origin of molecular attraction or repulsion:

1. **Electrostatic Energy (E_ele):** This component arises from Coulombic forces between charged or polar regions of the molecules. It reflects the attraction or repulsion due to the static distribution of partial charges (e.g., dipoles or ionic centers). A negative value indicates stabilizing attraction between opposite charges, while a positive value suggests repulsion.
2. **Polarization Energy (E_pol):** Polarization refers to the mutual distortion of electron clouds as molecules approach each other. When a molecule is influenced by the electric field of a neighboring molecule, its electron density may shift slightly, creating an induced dipole. This component typically contributes to stabilization but may be smaller than electrostatic or dispersion energies.
3. **Dispersion Energy (E_dis):** Also known as London dispersion forces, this energy stems from instantaneous dipole-induced dipole interactions. These are always attractive and arise even between non-polar molecules. In many organic crystals, dispersion forces are the dominant stabilizing interaction, particularly in systems lacking strong hydrogen bonds.
4. **Repulsion Energy (E_rep):** When molecules approach very closely, their electron clouds start to overlap, creating a strong repulsion. This happens because the Pauli exclusion principle prevents the simultaneous sharing of the same quantum state by electrons. Consequently, this repulsive energy is always positive and counters the attractive forces, helping to establish the stable separation between the molecules. These individual energies are combined into a total interaction energy (E_tot), which is a weighted sum of the components using empirically determined scaling factors: 1.057 for electrostatic, 0.740 for polarization, 0.871 for dispersion, and 0.618 for repulsion (according to the CE-B3LYP model). The dispersion energy network, shown in green, is the most widespread and concentrated, suggesting that dispersion forces play the leading role in maintaining the crystal's molecular arrangement. The electrostatic network, represented in red, features fewer connections, but these are oriented along key polar or dipolar regions, highlighting their directional importance. The total energy network, depicted in blue, merges all interaction types to reveal the main stabilizing routes within the crystal lattice. Notably, strong interactions along the b-axis appear as thick blue cylinders, corresponding to close contacts like the 7.07 Å interaction with a total energy of –64.6 kJ/mol (Fig.-8). These visual representations enhance the interpretation of the numerical energy values and validate the findings obtained through Hirshfeld surface analysis. They confirm that van

der Waals (dispersion) interactions and electrostatic forces are the dominant factors governing the stability and molecular packing patterns within the crystal structure.

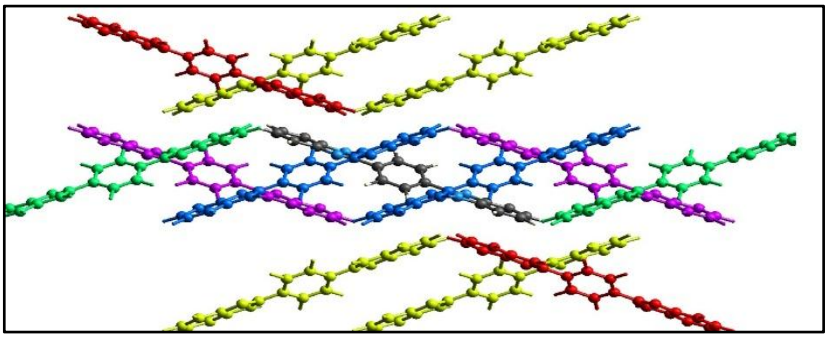

Fig.-8: Crystal Packing Viewed Along the Crystallographic *B*-Axis, Highlighting Spatial Arrangement of Molecules Within the Unit Cell. Molecules are Color-Coded According to Symmetry-Related Positions to Emphasize Packing Motifs and Intermolecular Interactions. This Orientation Corresponds to the Direction Used in the 3D Energy Framework Visualizations

To gain deeper insight into the spatial arrangement and comparative strength of intermolecular forces within the crystal lattice, three-dimensional energy frameworks were constructed. These models depict the energy landscape by mapping out interactions between molecular pairs using distinct color-coded cylinders corresponding to specific energy types: electrostatic energy (E_ele) is represented by red cylinders, dispersion energy (E_dis) by green cylinders, and the total interaction energy (E_tot) by blue cylinders. The diameter of each cylinder reflects the relative magnitude of the associated interaction energy, with thicker cylinders indicating stronger interactions. A cutoff radius of 3.8 Å was applied to identify the neighboring molecular fragments included in the energy calculations, ensuring accurate representation of short-range intermolecular forces (Fig.-9).

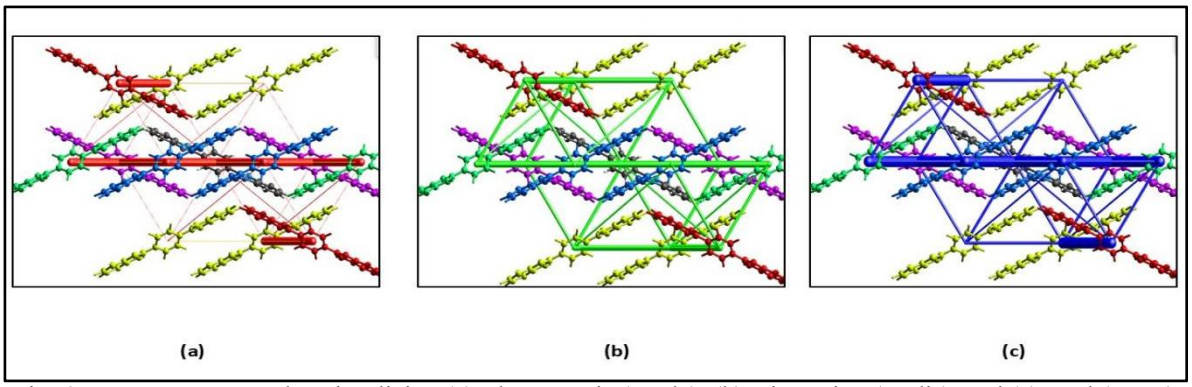

Fig.-9: Energy Frameworks Visualizing (a) Electrostatic (E_ele), (b) Dispersion (E_dis), and (c) total (E_tot) Interaction Energies. Cylinders Represent the Interaction Pathways, with Their Radii Scaled According to the Strength of the Energy Component. Red = E_ele, Green = E_dis, Blue = E_tot. Views are displayed along the Crystallographic *b*-axis

Calculated Interaction Energies

Table-1: Represents the Summary of the Interaction Energies between Selected Molecular Pairs in the Crystal, Including their Symmetry Relationship, Intermolecular Distance, and the Individual and Total Energy Components. Among the observed interactions, the most stabilizing interaction occurs between molecules related by the symmetry operation *x + 1/2, –y + 1/2, –z*, separated by 7.07 Å, with a total interaction energy of –64.6 kJ/mol. This strong stabilization is largely driven by electrostatic (–48.7 kJ/mol) and dispersion (–42.1 kJ/mol) forces. The polarization energy also contributes significantly, although the overall interaction is counterbalanced by a large repulsive component (42.5 kJ/mol), indicating close molecular proximity. Other notable interactions include a molecular pair at 9.09 Å (Symmetry: –x + ½; –y; z + 1/2) with –17.1 kJ/mol, dominated by dispersion forces. The identity operation pair (*x; y; z*) at 10.24 Å, showing 18.9

kJ/mol, is also primarily stabilized by dispersion energy. The weakest interaction occurs at 16.12 Å, where long-range dispersion contributes to a small stabilization of 3.4 kJ/mol. The calculated interaction energies confirm that dispersion interactions are the primary stabilizing force in the studied compound's crystal packing, followed by electrostatic interactions. This conclusion is consistent with visual and quantitative results from Hirshfeld surface analysis, particularly the 2D fingerprint plots, which further highlight the significance of van der Waals contacts in the crystal structure (Fig.-10).

Table-1: Interaction Energies and Symmetry Parameters of Molecular Dimers.

S. No.	Multiplicity	Symmetry Operation	Distance (Å)	Electron Density	Electrostatic	Polarization	Dispersion	Repulsion	Total Energy (kJ/mol)
	4	-x, y+1/2, z+1/2	13.61	B3LYP/6-31G(d,p)	-3.8	-1.5	-12.1	6	-10.9
	4	-x+1/2, -y, z+1/2	9.09	B3LYP/6-31G(d,p)	-1.7	-2.2	-21.5	6.8	-17.1
	4	x+1/2, -y+1/2, -z	16.12	B3LYP/6-31G(d,p)	0.8	-0.3	-6.3	2	-3.4
	4	x+1/2, -y+1/2, -z	7.07	B3LYP/6-31G(d,p)	-48.7	-17.6	-42.1	42.5	-64.6
	2	x, y, z	10.24	B3LYP/6-31G(d,p)	1.7	-2.9	-33.8	14.5	-18.9

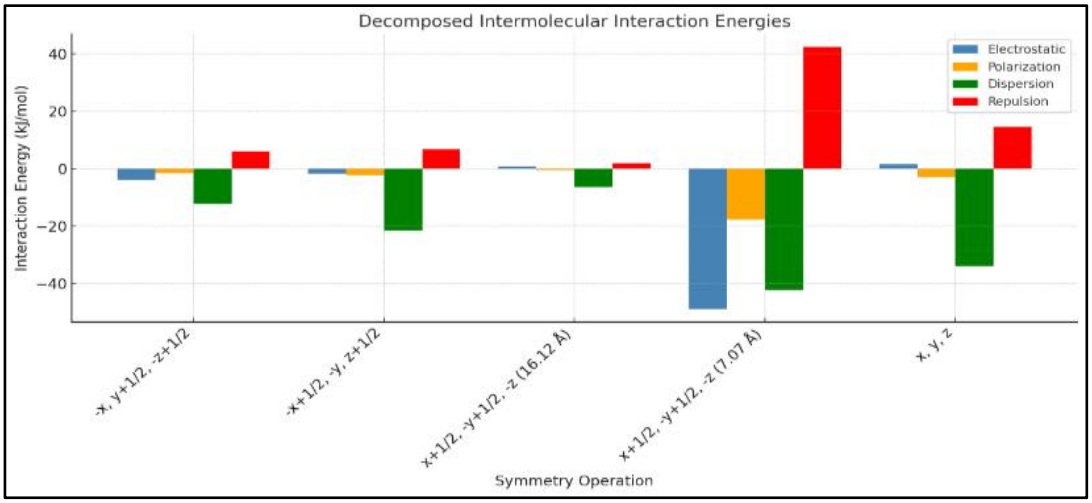

Fig.-10: Bar Chart Showing the Decomposition of Intermolecular Interaction Energies by Symmetry Operations

CONCLUSION

In summary, this study presents an efficient and environmentally benign one-pot synthetic route for the preparation of BBIB using CuBr as a Lewis acid catalyst and TTCA as a mild oxidant. The tandem catalytic system enables smooth integration of condensation, cyclization, and oxidative aromatization under mild conditions, achieving high yield and selectivity. Structural characterization through NMR, FTIR, and HRMS confirmed the identity as well as the purity of the synthesized compound. To analyse the supramolecular features of BBIB, comprehensive Hirshfeld surface analysis and intermolecular interaction energy calculations were performed, the results highlighted the dominance of dispersive

(H···H) interactions in crystal packing, complemented by significant C···H and N···H contacts that contribute to directional stabilization. Energy framework analysis further confirmed that dispersion forces are the primary stabilizing interactions, followed by electrostatic contributions. Altogether, this work not only demonstrates a green and practical synthetic strategy for bis-benzimidazole derivatives but also provides a detailed understanding of the intermolecular interactions governing their solid-state architecture. These findings could aid in the rational design of new functional materials or bioactive compounds based on benzimidazole frameworks.

CONFLICT OF INTERESTS

The authors declare that there is no conflict of interest.

AUTHOR CONTRIBUTIONS

The present work is related to *SDG-9: Industry, Innovation and Infrastructure*. All the authors contributed significantly to this manuscript, participated in reviewing/editing and approved the final draft for publication. The research profile of the authors can be verified from their ORCID ids, given below:

Lalima Sharma https://orcid.org/0009-0004-5550-043X
Siddhima Sharma https://orcid.org/0009-0008-8368-8459
Sonia Chahar Srivastava https://orcid.org/0000-0002-3352-2230
Mangal Shree Dulawat https://orcid.org/0000-0002-3666-2968

REFERENCES

1. O. Ebenezer, F. Oyetunde-Joshua, O. D. Omotoso, M. Shapi, *Results in Chemistry*, **5**, 100925 (2023), https://doi.org/10.1016/j.rechem.2023.100925
2. B. Pathare, T. Bansode, *Results in Chemistry*, **3**, 100200(2021), https://doi.org/10.1016/j.rechem.2021.100200
3. Salahuddin, M. Shaharyar, A. Mazumder, *Arabian Journal of Chemistry*, **10**, S157(2017), https://doi.org/10.1016/j.arabjc.2012.07.017
4. J. B. Moreira, J. Mann, S. Neidle, T. D. McHugh, P. W. Taylor, *International Journal of Antimicrobial Agents*, **42(4)**, 361(2013), https://doi.org/10.1016/j.ijantimicag.2013.04.033
5. K. Rajagopal, S. Dhandayutham, M. Nandhagopal, M. Narayanasamy, *Journal of Molecular Structure*, **1283**, 135253 (2023), https://doi.org/10.1016/j.molstruc.2023.135253
6. P. Kopel, D. Wawrzak, V. Langer, K. Cihalova, D. Chudobova, R. Vesely, V. Adam, R. Kizek, *Molecules*, **20(6)**, 10360(2015), https://doi.org/10.3390/molecules200610360
7. L. M. Aroua, F. M. Alminderej, H. R. Almuhaylan, A. H. Alosaimi, F. Medini, H. A. Mohammed, S. A. Almahmoud, R. A. Khan, N. H. Mekni, *RSC Advances*, **15(10)**, 7571(2025), https://doi.org/10.1039/D4RA08864F
8. A. G. Dale, J. Hinds, J. Mann, P. W. Taylor, S. Neidle, *Biochemistry*, **51(29)**, 5860(2012), https://doi.org/10.1021/bi300645n
9. M. Rashid, *Bioorganic Chemistry*, **96**, 103576 (2020), https://doi.org/10.1016/j.bioorg.2020.103576
10. M. A. Soliman, H. E. A. Ahmed, E. H. Eltamany, A. T. A. Boraei, A. Aljuhani, S. A. Salama, R. Alghamdi, A. K. B. Aljohani, M. Almaghrabi, M. A. Aouad, *Future Medicinal Chemistry*, **17(1)**, 93(2025), https://doi.org/10.1080/17568919.2024.2437980
11. M. Petit, J. Tessier, C. Sahli, A. R. Schmitzer, *ACS Infectious Diseases*, **9(11)**, 2202(2023), https://doi.org/10.1021/acsinfecdis.3c00289
12. Z. Šindelář, P. Kopel, *Inorganics*, **11(3)**, 113(2023), https://doi.org/10.3390/inorganics11030113
13. J. Sharma, P. K. Soni, R. Bansal, A. K. Halve, *Current Organic Chemistry*, **22(23)**, 2280(2018), https://doi.org/10.2174/1385272822666181024120156

14. S. I. Alaqeel, *Journal of Saudi Chemical Society*, **21(2)**, 229(2017), https://doi.org/10.1016/j.jscs.2016.08.001
15. Karthikeyan, M. P. Sibi, *Chiral Lewis Acids in Organic Synthesis*, Wiley, 2017, pp. 103–135, https://doi.org/10.1002/9783527802142.ch4
16. Z. Wu, M. Hu, Y. Jin, J. Li, W. Wu, H. Jiang, *Science Advances*, **7,** 35(2021), https://doi.org/10.1126/sciadv.abh4088
17. C. Dai, Z. Xu, F. Huang, Z. Yu, Y.–F. Gao, *Journal of Organic Chemistry*, **77(9)**, 4414(2012), https://doi.org/10.1021/jo202624s
18. R. P. van Summeren, A. Romaniuk, E. G. IJpeij, P. L. Alsters, *Catalysis Science & Technology*, **2(10)**, 2052 (2012), https://doi.org/10.1039/c2cy20403g
19. H. Yamaoka, N. Moriya, M. Ikunaka, *Organic Process Research & Development*, **8(6)**, 931(2004), https://doi.org/10.1021/op049940k
20. S. Gaspa, M. Carraro, L. Pisano, A. Porcheddu, L. De Luca, *European Journal of Organic Chemistry*, **2019(22)**, 3544(2019), https://doi.org/10.1002/ejoc.201900449
21. M. A. Spackman, D. Jayatilaka, *CrystEngComm*, **11(1)**, 19(2009), https://doi.org/10.1039/B818330A
22. P. R. Spackman, M. J. Turner, J. J. McKinnon, S. K. Wolff, D. J. Grimwood, D. Jayatilaka, M. A. Spackman, *Journal of Applied Crystallography*, **54(3)**, 1006(2021), https://doi.org/10.1107/S1600576721002910
23. P. C. Hariharan, J. A. Pople, *Theoretical Chemistry Accounts*, **28(3)**, 213(1973), https://doi.org/10.1007/BF00533485
24. A. D. Becke, *Journal of Chemical Physics*, **98(7)**, 5648(1993), https://doi.org/10.1063/1.464913

[RJC-9390/2025]